SCIENTIFIC REPORTS

OPEN

SUBJECT AREAS:
DENSITY FUNCTIONAL THEORY
THERMODYNAMICS

Received
16 January 2014

Accepted
7 May 2014

Published
28 May 2014

Correspondence and requests for materials should be addressed to G.C.W. (wang_guocheng@163.com)

Evidence of Multi-step Nucleation Leading to Various Crystallization Pathways from an Fe-O-Al Melt

G. C. Wang[1,2,3], Q. Wang[1,2], S. L. Li[1,2], X. G. Ai[1,2] & C. G. Fan[3]

[1]Key Laboratory of Chemical Metallurgy Engineering, Liaoning Province, University of Science and Technology Liaoning, Anshan, Liaoning, 114051, China, [2]School of Materials and Metallurgy, University of Science and Technology Liaoning, Anshan, 114051, China, [3]Jiangxi University of Science and Technology, Ganzhou, 341000, China.

The crystallization process from a solution begins with nucleation, which determines the structure and size of the resulting crystals. Further understanding of multi-pathway crystallizations from solution through two-step nucleation mechanisms is needed. This study uses density functional theory to probe the thermodynamic properties of alumina clusters at high temperature and reveals the thermodynamic relationship between these clusters and the saturation levels of dissolved oxygen and aluminum in an Fe–O–Al melt. Based on the thermodynamics of cluster formation and the experimental evidence for both excess oxygen in the Fe-O-Al melt and for alumina with a polycrystalline structure in solidified iron, we demonstrate that the appearance of various types of clusters that depends on the saturation ratio determines the nucleation steps that lead to the various crystallization pathways. Such mechanisms may also be important in nucleation and crystallization from solution.

Nucleation and crystallization from solution are fundamental to many industrial processes. Crystallization begins with nucleation, which plays a central role in determining the structure, shape and size distribution of the resulting crystals. Considering the shortcomings of classical nucleation theory (CNT), a mechanism for two–step nucleation (TSN) from solution[1–5] that includes multi-potential mechanisms[3,6,7] was recently proposed and supported by both experimental evidence of stable clusters[1,8–15] and by molecular simulation evidence of the clusters coming together[6,7,16–20] during nucleation. During TSN, sufficiently sized stable (or metastable) clusters of solute molecules form first, followed by the reorganization of these clusters into an ordered structure[3] during crystallization. The formation of liquid–like or amorphous precursors and even crystal–like configurations that differ from the final crystal are essential steps during nucleation[5,21–23]. However, the relationships between the various crystallization pathways and nucleation steps, which are important in controlling the structures and sizes of the resulting crystals, are still unclear and need to be studied and supported by experimental evidence.

Chemical reactions between dissolved elements in liquid iron that form condensed compounds are very common during the melting process. For example, a reaction occurs in which the aluminum (Al) and oxygen (O) dissolved in an Fe-O-Al melt form alumina products, usually α-Al_2O_3, to decrease the O content and to remove as much α-Al_2O_3 from the melt as possible. The stoichiometric reaction equation is $2Al + 3O = \alpha\text{-}Al_2O_3$, and the change in the standard Gibbs energy is[24,25] $\Delta_r G_m^{\Theta} = -1202.00 + 0.386T$, KJ·mol^{-1}. The process, simply described by CNT, is a heterogeneous reaction that results in the nucleation and crystallization of α-Al_2O_3. A supersaturated Fe–O–Al melt that contains O and Al is required to form α-Al_2O_3. The logarithm of the critical supersaturation ratio (log S*) was reported to be 3.5 using the electrochemical method[26], and this result was supported by CNT simulations[27].

The oxygen content measured following the reaction of Al with O in Fe-O-Al melts frequently exceeds the equilibrium level with respect to α-Al_2O_3[26–32]; however, the oxygen present as non-reactive oxygen continues to react with Al to form alumina products that are likely to remain in the solid material during cooling. The excess oxygen was hypothesized to originate from both the suspension of fine alumina products[29,30] and from the supersaturation of alumina-associated compounds[27,33]. Interestingly, however, the alumina products that were observed in solid samples prepared using ultra-rapid cooling at a rate of approximately 10^5 K/s are spherical with a diameter of a few to 10 nm or have a coral-like or network-like shape with a trunk thickness of approximately several hundred nanometers to a few micrometers, and these alumina products all have polycrystalline structures

consisting of α–, γ– and δ–alumina[34]. How can the excess oxygen and Al react to form products such as metastable γ– and δ–alumina during the ultra-rapid cooling process but retain their free status in the melt? Using CNT and Ostwald's step rule, it was concluded that these alumina products may form from the liquid alumina that appears during the initial stage of the reaction between Al and O, but determining whether liquid alumina is present in an Fe-O-Al melt is difficult[35].

Using TSN, our work calculates the thermodynamics of the nucleation of alumina from an Fe-O-Al melt and analyzes the relationships between the thermodynamics and the experimental evidence. Our results provide a clearer picture of multi-step nucleation that leads to various crystallization pathways from solution by using the thermodynamics of the formation of alumina clusters and the experimental evidence of both excess oxygen in an Fe–O–Al melt and alumina with a polycrystalline structure in solidified iron.

Results

Thermodynamic Properties. According to TSN, the formation of alumina products in an Fe–O–Al melt occurs as follows: During the first step, a population of alumina clusters, $(Al_2O_3)_n$ with n = 1–10, 15 and 30, form when Al reacts with O according to the equation $2\underline{Al} + 3\underline{O} = (1/n)(Al_2O_3)_n$, in which n is the number of Al_2O_3 units in a cluster. The second step is the crystallization of α–Al_2O_3 from $(Al_2O_3)_n$, which occurs according to the equation $(1/n)\ (Al_2O_3)_n = \alpha\text{–}Al_2O_3$.

In the current work, the thermodynamic properties of $(Al_2O_3)_n$ are simulated using density functional theory (DFT). The results show that the structures of $(Al_2O_3)_n$ (Figure S1 a) are in good agreement with the results of previous studies[36–37]. The apparent sizes of the $(Al_2O_3)_n$ clusters range from 0.410 nm to 1.690 nm (Figure S1 b). In the temperature range from 0 to 1000 K, the C_P (heat capacity), H (enthalpy) and S (entropy) of the $(Al_2O_3)_n$ clusters increase as the temperature increases (Figures S2 a, b, c). The G_V (vibrational free energy) and G (Gibbs free energy), however, decrease as the temperature increases (Figures 1a, b, d). Thus, the change in the thermodynamic properties of the $(Al_2O_3)_n$ clusters with temperature is similar to that in the bulk material. Furthermore, the C_P, H and S of the $(Al_2O_3)_n$ clusters increase with increasing n (Figures S2 a, b, c). There is a region in which the G_V curves intersect in the temperature range from 350 to 600 K (Figures 1a, b). Below the lower limit (350 K) of the temperature range, G_V increases with increasing n; this trend changes above the upper limit (600 K) to G_V decreasing with increasing n. This result indicates that the stability of the $(Al_2O_3)_n$ clusters changes with variations in the temperature. The zero-point energy, E (0 K), of the $(Al_2O_3)_n$ clusters decreases with increasing n (Figure 1c). In addition, the thermodynamic properties (C_P, S, H, G_V) of α-Al_2O_3 that are simulated using DFT are nearly consistent with the experimental data (C_P, S) in the temperature range from 0 to 1000 K[38] (Figure 2). The E (0 K) of α-Al_2O_3 is -1867993.697 KJ·mol^{-1}.

Thermodynamic Equilibrium. The formation of $(Al_2O_3)_n$ clusters is characterized using the equilibrium thermodynamics of the Fe–O–Al melt. In the second step, that is, $(1/n)\ (Al_2O_3)_n = \alpha\text{-}Al_2O_3$, $\Delta_rG_m^{\ominus}$ (S2) is given by $\Delta_rG_m^{\ominus}$ (S2) = $G_{\alpha\text{-}Al2O3} - (1/n)G_{(Al2O3)n}$. Using G = G_V + E (0 K), $\Delta_rG_m^{\ominus}$ (S2) is calculated as $\Delta_rG_m^{\ominus}$ (S2) = $(G_{V,\ \alpha\text{-}Al2O3} + E\ (0\ K)_{\alpha\text{-}Al2O3}) - (1/n)\ (G_{V,\ (Al2O3)n} + E\ (0\ K)_{(Al2O3)n})$. The fitted values of $\Delta_rG_m^{\ominus}$ (S2) with respect to temperature in the range of 0–1000 K are approximately linear (Table S2, right column); thus, the $\Delta_rG_m^{\ominus}$ (S2) values in the range of 1850–2000 K are the same as the fitted $\Delta_rG_m^{\ominus}$ (S2) values in the range of 0–1000 K (Figure S4 b). In the first step, that is, $2\underline{Al} + 3\underline{O} = (1/n)(Al_2O_3)_n$, $\Delta_rG_m^{\ominus}$ (S1) is given by $\Delta_rG_m^{\ominus}$ (S1) = $\Delta_rG_m^{\ominus} - \Delta_rG_m^{\ominus}$ (S2). The $\Delta_rG_m^{\ominus}$ (S1) values in the range of 1850–2000 K (which is the steelmaking temperature) are also given (Table S2, middle column; Figure S4 a). The results show that the $\Delta_rG_m^{\ominus}$ (S1) and $\Delta_rG_m^{\ominus}$ (S2) values are all negative in the range of 1850–2000 K; thus, the processes of cluster formation and α-Al_2O_3 crystallization can occur spontaneously. Furthermore, the formation of $(Al_2O_3)_n$ clusters is more likely than the crystallization of α-Al_2O_3 at a constant temperature of 1873 K (Figure S5) because the interfacial energy of the melt–liquid interface is considerably reduced relative to that of the melt–crystal interface, which results in a lower thermodynamic barrier to the formation of $(Al_2O_3)_n$ than to the crystallization of α-Al_2O_3.

Discussion

Thermodynamic Behavior of Alumina Clusters. To prove the existence of $(Al_2O_3)_n$ clusters and to elucidate the nucleation and crystallization pathways in an Fe-O-Al melt, the relationship between the experimental evidence and the thermodynamics is studied. Using the equation $2\underline{Al} + 3\underline{O} = (1/n)\ (Al_2O_3)_n$, the constant K′ can be written as $K' = 1/K = (a_{Al}{}^2a_O{}^3)/a_c = [f_{Al}\ (mass\%\ Al)_{eq}]^2 \cdot [f_O\ (mass\%\ O)_{eq}]^3/a_c$, in which K is the equilibrium constant; a_{Al}, a_O and a_c are the activities of Al, O, and $(Al_2O_3)_n$ in the melt, respectively; f_{Al} and f_O are the activity coefficients of Al and O, respectively; and $(mass\%\ Al)_{eq}$ and $(mass\%\ O)_{eq}$ are the mass fractions (%) of Al and O, respectively. In the standard state, the activity of $(Al_2O_3)_n$ is 1. The value of $f_{Al}{}^3 \cdot f_O{}^2$ is approximately 1 in a dilute Fe-O-Al melt. Thus, K′ can be written as $K' = (mass\%\ Al)^2_{eq} \cdot (mass\%\ O)^3_{eq}$. The equilibrium relationships between log [mass% Al] and log [mass% O] for the formation of $(Al_2O_3)_n$ at 1873 K in the present study are plotted as a group of colored solid curves ($c_O{}^c$) (Figure 3). The measured excess oxygen levels[28,30,31,39,40] are plotted as a scatter plot using symbols with various shapes. The critical value of the supersaturation ratio (S*) for the nucleation of α-Al_2O_3 was measured to be log S* = 3.5 using an electrochemical method[26] and was simulated as the log S = 3.5 curve and $c_O{}^{cr}$ value using CNT[27]; these values are plotted as a dotted curve and as a long dashed curve and solid curve, respectively (Figure 3, Figure S7). The relationship between Al and O in chemical equilibrium with α-Al_2O_3 and with its associated compound are plotted as a dotted curve ($c_O{}^{\alpha\text{-}Al2O3}$, inclined line) and as a short dashed curve with a large circle (the equilibrium curve), respectively[33] (Figure 3).

The $c_O{}^c$ curve of $(Al_2O_3)_1$ is located considerably higher than both the $c_O{}^{cr}$ curve and the experimental data of the excess oxygen from various studies. This result indicates that $(Al_2O_3)_1$ as a single molecule in an Fe–O–Al melt is unstable and easily transforms into other alumina clusters, $(Al_2O_3)_n$ with n > 1. The $c_O{}^c$ curves of $(Al_2O_3)_n$ with n > 1 and most of the measured values of the excess oxygen content are located in the region between the $c_O{}^{cr}$ and $c_O{}^{\alpha\text{-}Al2O3}$ curves. This result indicates that $(Al_2O_3)_n$ (n > 1) is present below the supersaturation level of the critical nucleus, and the presence of excess oxygen means that oxygen is in equilibrium with $(Al_2O_3)_n$ (n > 1) in the Fe-O-Al melt.

According to the experimental data of the excess oxygen with the $c_O{}^c$ curves of $(Al_2O_3)_n$ (n > 1), there are three types of alumina clusters in equilibrium with the excess oxygen in the Fe–O–Al melt (Figure 3). (I) Alumina clusters. In the cluster region of the $c_O{}^c$ curves, the stability of the clusters increases with a decrease in the excess oxygen level when the aluminum content (K′ decrease) and temperature are constant; thus, the clusters in this region are metastable and change with a variation in the excess oxygen level or temperature. (II) Alumina cluster aggregates. In the region between the $c_O{}^{cr}$ and $c_O{}^c$ curves of the most stable cluster, $(Al_2O_3)_8$, the clusters and the critical nucleus coexist. The alumina clusters in the Fe–O–Al melt, similar to clusters in a low-temperature solution[3,5,8], can effortlessly coalesce to form aggregates of various shapes and sizes. Thus, the excess oxygen in this region should be in equilibrium with alumina cluster aggregates that are smaller than the α-Al_2O_3 critical nucleus. Based on this finding, it is concluded that the alumina

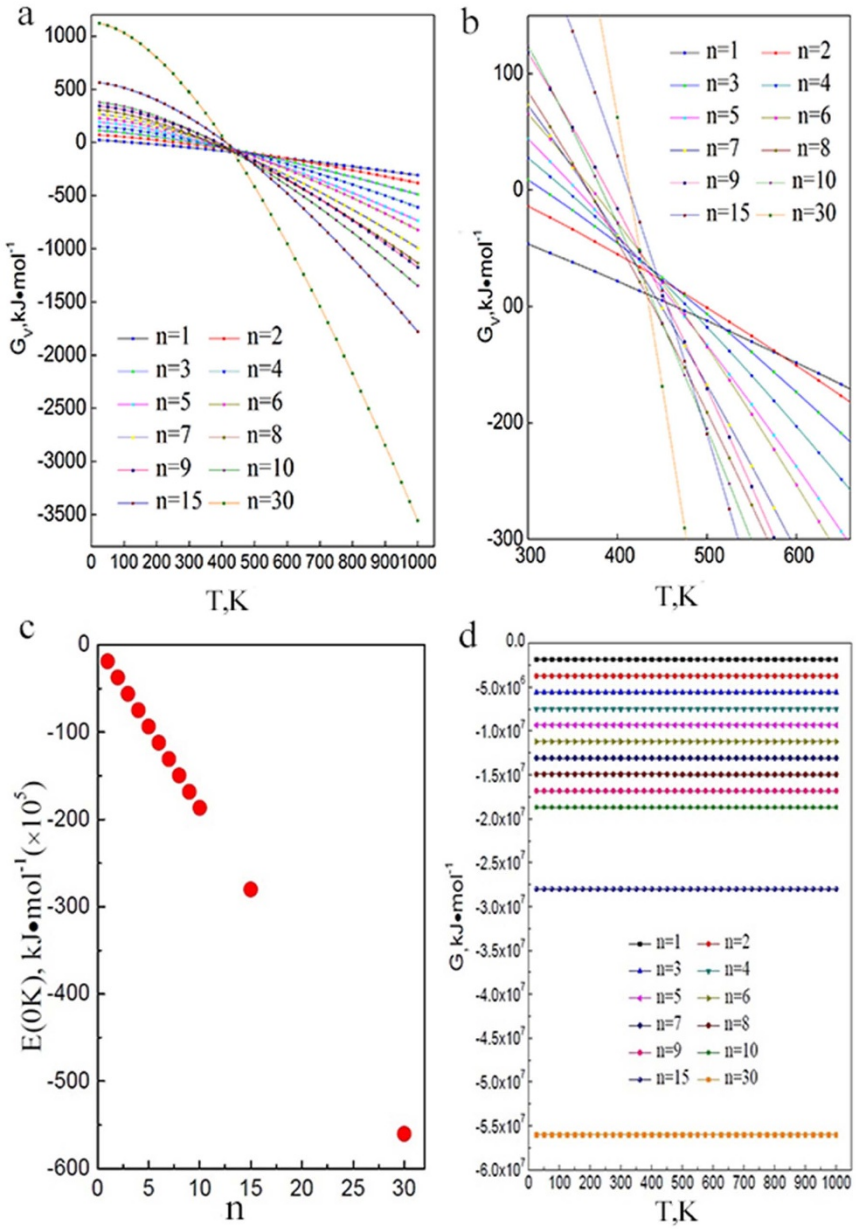

Figure 1 | The thermodynamic properties of $(Al_2O_3)_n$ with n = 1–10, 15 and 30 at 0–1000 K. (a) The values of the vibrational free energy, G_V, of $(Al_2O_3)_n$ are plotted as a group of colored solid curves. (b) A magnified section of (a) in the region of the intersection of the G_V values of $(Al_2O_3)_n$. The temperature range of the region of the intersection is approximately 350 K to 600 K. (c) The zero-point energy at a temperature of 0 K, E (0 K). (d) The Gibbs free energy, G, where G = G_V + E (0 K).

cluster aggregates are unstable and spontaneously appear depending on the degree of saturation of O and Al in the melt. Thus, the sizes of the alumina products, which have various shapes, are considerably larger than the maximum size of a cluster [$(Al_2O_3)_{30}$, 1.690 nm]. (III) Crystal-like clusters. In the region between the $c_O{}^c$ curve of the most stable cluster and the $c_O{}^{\alpha\text{-}Al2O3}$ curve, the clusters and the α-Al_2O_3 coexist. Therefore, the excess oxygen in this region should be in equilibrium with crystal–like clusters that are more stable than the clusters in the melt, similar to the crystal–like clusters in a low-temperature solution[3,5]. These results indicate that various species of clusters, including alumina clusters, cluster aggregates and crystal-like clusters, could be present and in equilibrium with the excess oxygen in an Fe–O–Al melt. Thus, we conclude that "the excess oxygen" is not really excess oxygen but rather the oxygen in equilibrium with various alumina clusters (hereafter referred to as the equilibrium oxygen with clusters) in the melt.

Multi-step Nucleation Leading to Various Crystallization Pathways. Based on Ostwald's step rule, clusters of various species form a series of transitional phases in the process of Al reacting with O. If the saturation ratios of Al and O are higher than that of the formation of critical nuclei (log S^*_{cr} = 3.5, 1873 K, $\Delta_r G_m^{\ominus}$ = −354.169, KJ·mol^{-1}), as with S_1, there is a multi-step nucleation process in the Fe–O–Al melt in which Al and O first react to form $(Al_2O_3)_n$, and then, the clusters coalesce to form aggregates; eventually, the aggregates crystallize into the critical nucleus, which is followed by the immediate and spontaneous growth of α-Al_2O_3 (1873 K, $\Delta_r G_m^{\ominus}$ = −479.688 KJ·mol^{-1}) during the reaction (Figure 4). However, if the saturation ratio is lower than S^*_{cr} and higher than that of aggregate formation (S^*_{ag}), as with S_2, the cluster aggregates cannot crystallize into the critical nucleus in the melt. In this case, the crystallization of α-Al_2O_3 cannot progress further at the steelmaking temperature; thus, equilibrium oxygen with clusters is

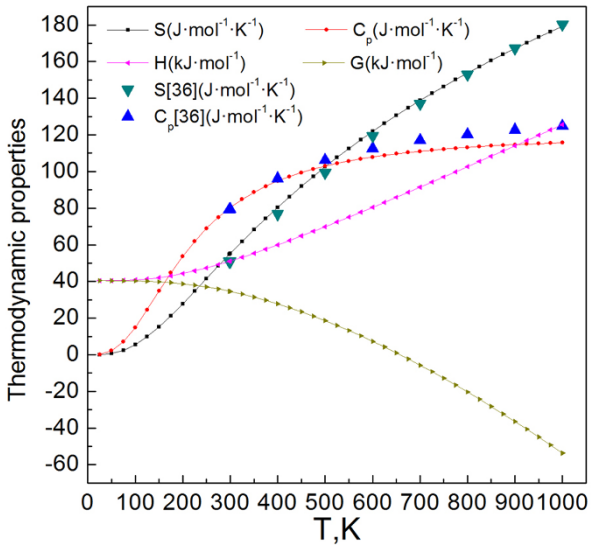

Figure 2 | The thermodynamic properties of the α-Al_2O_3 crystal. The experimental values[38] of C_P and S are plotted as blue and green triangles, respectively. The values of C_P, S, H and G_V that were simulated using DFT are plotted as colored solid curves.

present in the post-reaction melt. If the saturation degree is lower than S^*_{ag} and higher than that of cluster formation (S^*_{cl}, 1873 K, the most stable cluster, $(Al_2O_3)_8$, $\Delta_r G_m^{\ominus} = -381.056$ KJ·mol^{-1}), as with S_3, the clusters cannot coalesce and form aggregates in the melt. If the degree of saturation is lower than S^*_{cl}, as with S_4, the Al and O cannot react to form $(Al_2O_3)_n$ and there are only crystal–like clusters in the Fe–O–Al melt (Figure 4). We conclude that during cooling, various species of clusters in the post-reaction Fe–O–Al melt can only crystallize directly into alumina with different shapes, sizes and polycrystalline structures that consist of α–, γ– and δ–Al_2O_3 because the equilibrium thermodynamics change with the decrease in temperature (Figure S10). In other words, the morphologies and structures of the alumina products in solid steel could strongly depend on the various species of clusters in the melt.

Because of these findings, we argue that stable clusters could be present in an Fe-O-Al melt. In a melt with a high saturation ratio, alumina clusters can coalesce and form aggregates that then change into critical nuclei, leading to the crystallization of α-Al_2O_3 during the reaction of aluminum with oxygen. In a post-reaction Fe–O–Al melt, various species of alumina clusters are present depending on the saturation ratio, and they cannot crystallize into the critical nuclei of α-Al_2O_3 but rather crystallize directly into various structural alumina products (γ–, δ–Al_2O_3) as the temperature decreases during the cooling stage. A greater understanding of the multi-step nucleation that leads to the various crystallization pathways may lead to the design of auxiliaries that can control the rate of nucleation and avoid the formation of undesired solid forms.

Methods

All the simulations for calculating the thermodynamic properties in the present work are performed using DFT with the molecular orbital theory computational program Dmol^3. The initial structures are established using the Visualizer module of MS 6.0. The geometry optimization is performed using the BFGS (the abbreviation corresponds to the first letters of the names of the following researchers: Broyden, Fletcher, Goldfarb, and Shanno) method with a quasi-Newton algorithm. The hybrid density functional BLYP (the abbreviation corresponds to the first letters of the names of the following researchers: Becke, Lee, Yang and Parr) method using a generalized gradient approximation (GGA) is used as the exchange-correlation potential function. The thermodynamic properties of various structures are calculated using the atomic harmonic vibrational frequency based on statistical thermodynamics. The initial structures of the alumina clusters, $(Al_2O_3)_n$ with n = 1–10, 15 and 30, are established using Visualizer. The precision of BFGS is set as follows: energy ≤ 2.0×10^{-5} Ha, tension ≤ 0.004 Ha/Å, and shift ≤ 0.005 Å. The self-consistent field (SCF) method is used with the precision of the total energy and charge density set at 1×10^{-5} Ha, and the thermal smearing effect is used at a precision of 0.005 Ha. The cut-off radius of the DNP basis set of the *d* orbital is 3.5 Å. Electrons outside the atomic nucleus are handled using the effective core potentials (ECP) method. The initial structure of the

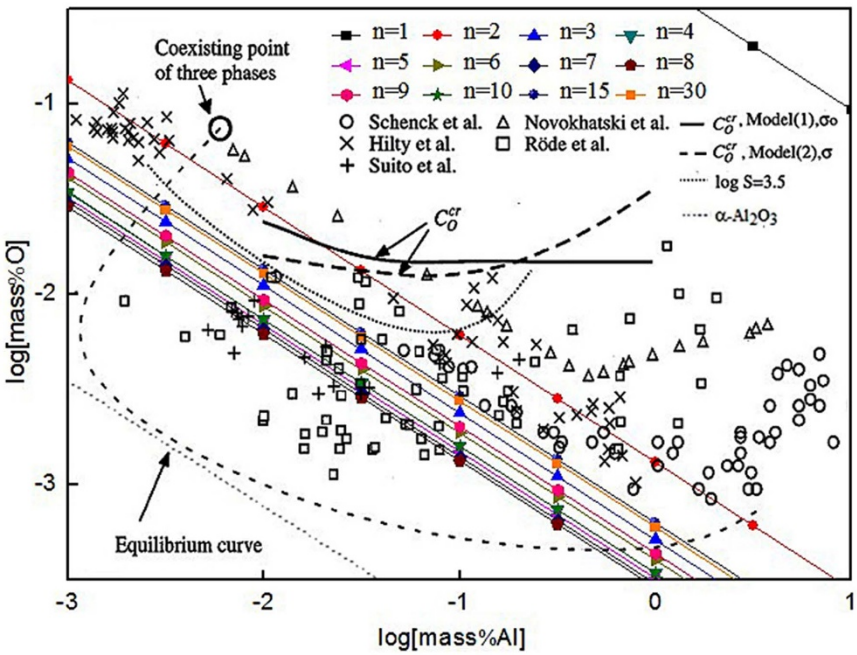

Figure 3 | The relationship between log (mass% Al) and log (mass% O) at 1873 K. The equilibrium relationships between $(Al_2O_3)_n$ and Al and O in an Fe-O-Al melt are plotted as a group of colored solid curves (c_O^c). The measured values of excess oxygen[28,30,31,39,40] are plotted as a scatter plot using symbols with various shapes. The critical value of the supersaturation ratio (S*) of α-Al_2O_3 nucleation was measured to be log S* = 3.5 using an electrochemical method[26] and was simulated as the c_O^{cr} value using CNT[27]; these values are plotted as a dotted curve and as a long dashed curve and solid curve, respectively. The relationships of Al and O in chemical equilibrium with α-Al_2O_3 and with its associated compound are plotted as a dotted curve ($c_O^{\alpha\text{-}Al2O3}$, inclined line) and as a short dashed curve with a large circle (the equilibrium curve), respectively[33].

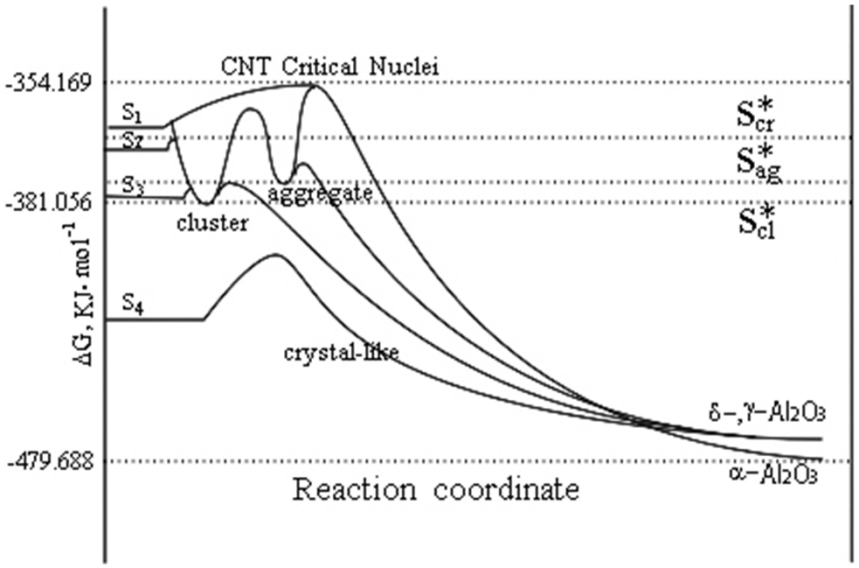

Figure 4 | A schematic illustration of the nucleation and crystallization from the melt. S^*_{cr} is the critical degree of saturation at which the critical nuclei form. S^*_{ag} is the critical degree of saturation at which the cluster aggregates form. S^*_{cl} is the critical degree of saturation at which the alumina clusters form. The melt in the S1 state can form critical nuclei and crystallize into alumina products, that is, α-Al_2O_3 in an Fe-O-Al melt, and the multi-step nucleation process is shown as a solid red curve. However, S_2, S_3 and S_4 can only form alumina products that are dependent on the crystallization process during cooling of the post-reaction melt, and the multi-pathways to crystallization are shown as solid black curves.

α-Al_2O_3 crystal is adopted from the MS 6.0 structural database. The precision of the BFGS algorithm is set as follows: energy $\leq 2.0 \times 10^{-5}$ Ha, tension ≤ 0.004 Ha/Å, and shift ≤ 0.005 Å. The Brillouin zone integral is calculated using the Monkhorst_Pack method with a grid size of $3 \times 3 \times 2$ k-points. The precision of the total energy and charge density is set as 1×10^{-5} Ha, and the thermal smearing effect is used at a precision of 0.055 Ha. The cut-off radius of the DNP basis set of the *d* orbital is 3.5 Å. Electrons outside the atomic nucleus are handled using the ECP method.

1. Vekilov, P. G. Dense liquid precursor for the nucleation of ordered solid phases from solution. *Cryst. Growth Des.* **4**, 671–685 (2004).
2. Vekilov, P. G. Two-step mechanism for the nucleation of crystals from solution. *J Cryst Growth.* **275**, 65–76 (2005).
3. Erdemir, D., Lee, A. Y. & Myerson, A. S. Nucleation of Crystals from Solution: Classical and Two-Step Models. *Acc. Chem. Res.* **42**, 621–629 (2009).
4. Vekilov, P. G. The two-step mechanism of nucleation of crystals in solution. *Nanoscale.* **2**, 2346–2357 (2010).
5. Myerson, A. S. & Bernhardt, L. T. Nucleation from Solution. *Science* **341**, 855–856 (2013).
6. Vekilov, P. G. Nucleation. *Cryst. Growth Des.* **10**, 5007–5019 (2010).
7. Sear, R. P. The non-classical nucleation of crystals: microscopic mechanisms and applications to molecular crystals, ice and calcium carbonate. *Int. Mater. Rev.* **57**, 328–356 (2012).
8. Gebauer, D., Völkel, A. & Cölfen, H. Stable Prenucleation Calcium Carbonate Clusters. *Science* **322**, 1819–1822 (2008).
9. Igarashi, K., Azuma, M., Kato, J. & Ioshima, H. The Initial Stage of Crystallization of Lysozyme: A Differential Scanning Calorimetric (DSC) Study. *J. Cryst. Growth.* **204**, 181–200 (2006).
10. Knezic, D., Zaccaro, J. & Myerson, A. S. Nucleation induction time in levitated droplets. *J. Phys. Chem. B.* **108**, 10672–10677 (2004).
11. Galkin, O., Chen, K., Nagel, R. L., Hirsch, R. E. P. & Vekilov, G. Liquid-Liquid Separation in Solutions of Normal and Sickle Cell Hemoglobin. *Proc. Natl. Acad. Sci. U.S.A.*, **99**, 8479–8483 (2002).
12. Chattopadhyay, S. *et al.* SAXS Study of the Nucleation of Glycine Crystals from a Supersaturated Solution. *Cryst. Growth Des.* **5**, 523–527 (2005).
13. Zaccaro, J., Matic, J., Myerson, A. S. & Garetz, B. A. Nonphotochemical, Laser-Induced Nucleation of Supersaturated Aqueous Glycine Produces Unexpected γ-polymorph. *Cryst. Growth Des.* **1**, 5–8 (2001).
14. Garetz, B., Matic, J. & Myerson, A. S. Polarization Switching of Crystal Structure in the Nonphotochemical Light-Induced Nucleation of Supersaturated Aqueous Glycine Solutions. *Phys. Rev. Lett.* **89**, 175501.1–4 (2002).
15. Emilie, M. *et al.* The Initial Stages of Template-Controlled $CaCO_3$ Formation Revealed by Cryo-TEM. *Science.* **323**, 1455–1458 (2009).
16. Wallace, A. F. *et al.* Microscopic Evidence for Liquid-Liquid Separation in Supersaturated $CaCO_3$ Solutions. *Science.* **341**, 885–889 (2013).
17. Demichelis, R., Raiteri, P., Gale, J. D., Quigley, D. & Gebauer, D. Stable prenucleation mineral clusters are liquid-like ionic polymers. *Nat. Commun.* **2**, 1–8 (2011).
18. Raiteri, P. & Gale, J. D. Water Is the Key to Nonclassical Nucleation of Amorphous Calcium Carbonate. *J. Am. Chem. Soc.* **132**, 17623–17634 (2010).
19. Gebauer, D. *et al.* Proto-calcite and proto-vaterite in amorphous calcium carbonates. *Angew. Chem. Int. Ed. Engl.* **49**, 8889–8891 (2010).
20. Ten Wolde, P. R. & Frenkel, D. Enhancement of Protein Crystal Nucleation by Critical Density Fluctuations. *Science.* **277**, 1975–1978 (1997).
21. Ten Wolde, P. R., Ruiz-Montero, M. J. & Frenkel, D. Numerical Evidence for bcc Ordering at the Surface of a Critical fcc Nucleus. *Phys. Rev. Lett.* **75**, 2714–2717 (1995).
22. Lechner, W., Dellago, C. & Bolhuis, P. G. Reaction coordinates for the crystal nucleation of colloidal suspensions extracted from the reweighted path ensemble. *J. Chem. Phys.* **135**, 154110–154123 (2011).
23. Giberti, F., Tribello, G. A. & Parrinello, M. Transient Polymorphism in NaCl. *J. Chem. Theory Comput.* **9**, 2526–2530 (2013).
24. Sigworth, G. K. & Elliott, J. F. The Thermodynamics of Liquid Dilute Iron Alloys. *Met. Sci.* **8**, 298–310 (1974).
25. Elliott, J. F., Gleiser, M. & Ramakrishna, V. *Thermochemistry for Steelmaking* [67] (Addison-Wesley Publishing Co., Reading, MA, 1963), vol.2.
26. Li, G. & Suito, H. Electrochemical Measurement of Critical Supersaturation in and Fe-O-M (M=Al. Si, and Zr) and Fe-O-Al-M (M=C, Mn, Cr, Si, and Ti) Melts by Solid Electrolyte Galvanic Cell. *Iron Steel Inst. Jpn. Int.* **37**, 762–769 (1997).
27. Waai, K. & Mukai, K. Thermodynamics of Nucleation and Supersaturation for the Aluminum-Deoxidation Reaction in Liquid Iron. *MMTB.* **30**, 1065–1074 (1999).
28. Suito, H., Inoue, H. & Inoue, R. Aluminium-Oxygen Equilibrium between CaO-Al_2O_3 Melts and Liquid Iron. *ISIJ International.* **31**, 1381–1388 (1991).
29. Repetylo, O., Olette, M. & Kozakevitch, P. Deoxidation of Liquid Steel with Aluminum. *J. Met.* **19**, 45–49 (1967).
30. Rohde, L. E., Choudhury, A. & Wahlster, M. New Investigations on the Al-O Equilibrium in Iron Melts. *Arch Eisenhüttenwes.* **42**, 165–174 (1971).
31. Schenck, H., Steinmetz, E. & Mehta, K. K. Equilibria and Kinetics of the Separation of Alumina from the Iron-Oxygen-Aluminum System at 1600°C. *Arch Eisenhüttenwes.* **41**, 131–138 (1970).
32. Fitterer, G. R. Proc. American Institute of Mining and Metallurgy, Petroleum Engineers National Open Hearth Basic Oxygen Steel Conf. **59**, 212–226 (1976).
33. Waai, K. & Mukai, K. Thermodynamic Analysis of Fe-Al-O Liquid Alloy Equilibrated with α-$Al_2O_{3(s)}$ by an Associated Solution Model. *J. Japan Inst. Metals.* **52**, 1088–1097 (1988).
34. Waai, K., Mukai, K. & Akifumi, M. Observation of Inclusion in Aluminum Deoxidized Iron. *ISIJ International.* **42**, 459–466 (2002).
35. Waai, K. & Mukai, K. Thermodynamic Analysis on Metastable Alumina Formation in Aluminum Deoxidized Iron Based on Ostwald's Step Rule and Classical Homogeneous Nucleation Theories. *ISIJ International.* **42**, 467–473 (2002).
36. Amol, B. R., Mrinalini, D. D. & Vijay, K. Structural and Electronic Properties of $(Al_2O_3)_n$ Clusters with n = 1–10 from First Principles Calculations. *J. Phys. Chem. C.* **115**, 18111–18121 (2011).
37. Sun, J. *et al.* Theoretical study on $(Al_2O_3)_n$ (n = 1-10 and 30) fullerenes and H_2 adsorption properties. *Inorganic chemistry.* **47**, 2274–2279 (2008).

38. Ihsan, B. *Thermochemical Data of Pure Substances* [48–48] (VCH Verlagsgesellschaft mbH, D-69451 Weinheim, Federal Republic of Germany, 1995). [third edition].
39. Hilty, D. C. & Crafts, W. The solubility of oxygen in liquid iron containing aluminum. *J. Met. Trans. AIME.* **188**, 414–424 (1950).
40. Novokhatskiy, I. A. & Belov, B. F. Concentration Dependence of the Solubility of Oxygen in Alloys. *Izv. Akad. Nauk SSSR Met.* **3**, 15–26 (1969).

Acknowledgments

The authors are grateful for the financial support from the National Natural Science Foundation of China (grant 51004054).

Author contributions

G.W. and Q.W. proposed this research and wrote the paper with contributions from all the authors. G.W. performed the first principles calculations. S.L., X.A. and C.F. helped with the data analysis and discussion. G.W. supervised the projects.

Additional information

Supplementary information accompanies this paper at http://www.nature.com/scientificreports

Competing financial interests: The authors declare no competing financial interests.

How to cite this article: Wang, G.C., Wang, Q., Li, S.L., Ai, X.G. & Fan, C.G. Evidence of Multi-step Nucleation Leading to Various Crystallization Pathways from an Fe-O-Al Melt. *Sci. Rep.* **4**, 5082; DOI:10.1038/srep05082 (2014).